Structure of synthetic monoclinic Na-rich birnessite and hexagonal birnessite: I. Results from X-ray diffraction and selected-area electron diffraction

VICTOR A. DRITS,[1] EWEN SILVESTER,[2,]* ANATOLI I. GORSHKOV,[3] AND ALAIN MANCEAU[2]

[1]Geological Institute of the Russian Academy of Sciences, 7 Pyzhevsky Street, 109017 Moscow, Russia
[2]Environmental Geochemistry Group, LGIT-IRIGM, University of Grenoble and CNRS, 38041 Grenoble Cedex 9, France
[3]Institute of Ore Mineralogy of the Russian Academy of Science, 35 Staromonetny Street, 109017, Moscow, Russia

ABSTRACT

Synthetic Na-rich birnessite (NaBi) and its low pH form, hexagonal birnessite (HBi), were studied by X-ray and selected-area electron diffraction (XRD, SAED). SAED patterns were also obtained for synthetic Sr-exchanged birnessite (SrBi) microcrystals in which Sr was substituted for Na. XRD confirmed the one-layer monoclinic structure of NaBi and the one-layer hexagonal structure of HBi with subcell parameters $a = 5.172$ Å, $b = 2.849$ Å, $c = 7.34$ Å, $\beta = 103.3°$ and $a = 2.848$ Å, $c = 7.19$ Å, $\gamma = 120°$, respectively. In addition to super-reflection networks, SAED patterns for NaBi and SrBi contain satellite reflections.

On the basis of these experimental obervations, structural models for NaBi and HBi are proposed. NaBi consists of almost vacancy-free Mn octahedral layers. The departure from the hexagonal symmetry of layers is caused by the Jahn-Teller distortion associated with the substitution of Mn^{3+} for Mn^{4+}. The supercell $A = 3a$ parameter arises from the ordered distribution of Mn^{3+}-rich rows parallel to [010] and separated from each other along [100] by two Mn^{4+} rows. The superstructure in the b direction of NaBi type II ($B = 3b$) comes from the ordered distribution of Na cations in the interlayer space. The maximum value of the layer negative charge is equal to 0.333 v.u. per Mn atom and is obtained when Mn^{3+}-rich rows are free of Mn^{4+}. The idealized structural formula proposed for NaBi type II is $Na_{0.333}(Mn^{4+}_{0.722}Mn^{3+}_{0.222}Mn^{2+}_{0.055})O_2$. NaBi type I has a lower amount of Mn^{3+} and its ideal composition would vary from $Na_{0.167}(Mn^{4+}_{0.833}Mn^{3+}_{0.167})O_2$ to $Na_{0.25}(Mn^{4+}_{0.75}Mn^{3+}_{0.25})O_2$. Satellites in SAED patterns of NaBi crystals result from the ordered distribution of Mn^{4+} and Mn^{2+} pairs in Mn^{3+}-rich rows with a periodicity of $6b$.

The structure of HBi consists of hexagonal octahedral layers containing predominantly Mn^{4+} with variable amounts of Mn^{3+} and layer vacancies. The distribution of layer vacancies is inherited from the former Mn^{3+} distribution in NaBi. Interlayer Mn cations are located above or below vacant layer sites. The driving force of the NaBi to HBi transformation is probably the destabilization of Mn^{3+}-rich rows at low pH.

INTRODUCTION

Birnessite belongs to the phyllomanganate family. The first occurrence of this mineral was reported by Jones and Milne (1956) among black grains in the Birness Region (Scotland). The following chemical formula was proposed: $Na_{0.7}Ca_{0.3}Mn_7O_{14}\cdot2.8H_2O$. More recently it has been recognized that birnessite occurs in various geological environments and can form under different physicochemical conditions. This mineral is the main Mn-bearing phase in soils (Taylor et al. 1964; Chukhrov and Gorshkov 1981; Cornell and Giovanoli 1988) and in marine and ocean manganese nodules and micronodules (Burns and Burns 1976; Chukhrov and Gorshkov 1981; Chukhrov et al. 1978, 1985, 1989; Glover 1977; Drits et al.

1985). Birnessite is also a major component of some Mn-rich ore deposits (Chukhrov et al. 1987, 1989; Usui and Mita 1995). Birnessite possesses unique surface charge (Healy et al. 1966; Murray 1974), cation exchange (Balistrieri and Murray 1982; Le Goff et al. 1996), and redox (Stone et al. 1994) properties, which make it highly reactive with respect to sorption phenomena (Tu et al. 1994; Paterson et al. 1994). Furthermore, birnessite is synthesized easily under laboratory conditions (Giovanoli et al. 1970a, 1970b; Bricker 1965; Strobel et al. 1987; Cornell and Giovanoli 1988) and, consequently, often has been used as a model manganese oxide in environmental chemical studies (Stone and Morgan 1984; Stone 1987; Xyla et al. 1992; Manceau and Charlet 1992; Bidoglio et al. 1993).

Despite the fact that the main structural and chemical properties of natural (Chukhrov et al. 1985, 1989; Man-

ceau et al. 1992) and synthetic (Post and Veblen 1990; Kuma et al. 1994) birnessite has been determined, many details concerning its structure and crystal chemistry remain poorly understood, specifically diffraction features, crystal-chemical formula, and physico-chemical properties for the different individual birnessite species, and the structural mechanism of their formation and transformation. The solution to the first two problems predetermines the success in the solution of the others.

The present paper and the companion paper (Silvester et al. 1997) deal with the structure of synthetic Na-rich birnessite and its modifications that occur under acidic alteration. This paper is concerned with structural information obtained from X-ray diffraction (XRD) and selected-area electron diffraction (SAED). The second paper presents the results of extended X-ray absorption fine structure (EXAFS) analysis and chemical studies. All these new results will be discussed in the light of data previously reported in the literature to obtain a more comprehensive understanding of birnessite structure.

PREVIOUS STRUCTURAL STUDIES

One of the main difficulties in the structural study of birnessite is that it exhibits several natural and synthetic varieties. Furthermore, it occurs in an extremely dispersed state and generally has a low degree of structural perfection. For these reasons, until recently, even the unit-cell parameters of the various described birnessite modifications were not determined unambiguously. Giovanoli et al. (1970a) and Burns and Burns (1977) proposed that the birnessite structure is analogous to that of chalcophanite ($ZnMn_3O_7 \cdot 3H_2O$; Wadsley 1955; Post and Appleman 1988). In each chalcophanite layer one out of seven Mn^{4+} octahedral sites is vacant. Vacant sites form a superstructure with the layer unit-cell parameters: $a = b = 7.54$ Å and $\gamma = 120°$. Interlayer Zn cations are located above and below vacant Mn sites. Based on a close anion packing notation this structure can be expressed as AbCb′A′c′BcAc′B′a′CaBa′C′b′AbC, where A, B, and C represent sites for O atoms; A′, B′, and C′ sites for H_2O molecules; a, b, and c layer Mn sites; and a′, b′, and c′ interlayer sites.

Burns and Burns (1977) speculated that interlayer alkali and alkaline earth cations occupy the same positions in the birnessite structure as Zn^{2+} cations in chalcophanite. Giovanoli and Arrhenius (1988) proposed that in birnessite layers one out of six Mn sites is vacant and that Mn^{2+} and Mn^{3+} cations occupy interlayer sites above and below layer vacancies. A vacancy model for phyllomanganates was also developed by Strobel et al. (1987). All these models are based on intuitive considerations deduced from the determination of unit-cell parameters without any quantitative analysis of the diffraction patterns.

Hexagonal one-layer birnessite

The first detailed structural study of natural birnessite was performed by Chukhrov et al. (1985) using XRD and SAED. This pure birnessite sample came from manganese micronodules dredged from the Pacific Ocean floor. This sample had a hexagonal unit cell with $a = 2.838$ and $c = 7.10$ Å. Using the same symbolic notation as for chalcophanite, the layer sequence for the model structure suggested by Chukhrov et al. (1985) is:

$$AbCb′\overset{A'}{\underset{C'}{}}b′AbC$$
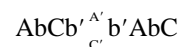
This interpretation was supported by X-ray absorption spectroscopy (Manceau et al. 1992). The structural analogy with the chalcophanite structure was then established on a quantitative basis, both minerals having similar layer and interlayer structures, but with birnessite exhibiting a one-layer hexagonal cell and a random distribution of vacancies within the layer. Those XRD patterns of synthetic and natural birnessites with a hexagonal unit cell described by Giovanoli et al. (1976) and Glover (1977) are similar to that of Chukhrov et al. (1985).

Birnessite with monoclinic subcell

One occurrence of natural one-layer monoclinic birnessite has been reported by Gorshkov et al. (1992). The structure of synthetic monoclinic birnessite samples containing exchangeable Na^+, Mg^{2+}, and K^+ cations in their interlayer was determined for the first time by Post and Veblen (1990) using the Rietveld technique. The results obtained by these authors confirmed the similarity of synthetic birnessite and chalcophanite structures. These birnessite samples have a monoclinic subcell, the shape and size of which varies with the nature of the interlayer cations. The idealized one-layer monoclinic structure of Na-rich birnessite (NaBi) may be transformed into a three-layer rhombohedral structure, the layer sequence of which may be compared with that of chalcophanite (Manceau et al. 1992):

AbC CaB BcA AbC   NaBi (monoclinic)

AbC BcA CaB AbC   chalcophanite

For the sake of simplicity only the stack of Mn octahedral layers is represented here. The minerals differ by their layer stacking and, consequently, do not possess the same interlayer structure. In agreement with the pure layered structure found by Post and Veblen (1990), no Mn-O-Mn corner linkages were detected by EXAFS in the synthetic monoclinic NaBi sample (Manceau et al. 1992).

Origin of birnessite superstructures

Giovanoli et al. (1970a) were the first to observe the existence of superreflections in the SAED pattern of synthetic NaBi. They assumed that these superstructures were caused by an ordering of Mn vacancies as for chalcophanite. Similar conclusions were drawn by Chukhrov et al. (1978) from the SAED and energy-dispersive analysis (EDA) study of Ca-rich oceanic micronodules.

From the analysis of SAED patterns, Post and Veblen (1990) concluded that it was most likely that superreflec-

tions resulted from a regular distribution of interlayer cations rather than of vacancies. This was supported by the fact that Na-rich and Mg-exchanged birnessite had different superstructures but the same layer charge. Manceau et al. (1992) proposed that the two dimensional superperiodicity observed in the SAED patterns for NaBi particles resulted from a periodic distribution of Na$^+$ atoms because of their electrostatic interactions. Accordingly, the exchange of Na$^+$ by Mg^{2+} should lead to a new superperiodicity because of the decrease of the number of interlayer cations. This effect was actually observed by Post and Veblen (1990). However, according to these authors, Mg^{2+} atoms in Mg-exchanged birnessite, hereafter referred to as MgBi, are located almost above or below octahedral sites. Such an arrangement of interlayer Mg^{2+} cations is possible only if the underlying sites are vacant (Manceau et al. 1992). This observation must be considered as a strong argument in favor of layer vacancies in the structure of monoclinic birnessite. Thus, there is a contradiction in the data presented by Post and Veblen (1990). On the one hand, SAED data and the constancy of the interlayer charge for Na and Mg birnessite support the idea that the superstructure results from the ordered distribution of interlayer species. On the other hand, the structural refinement of MgBi indicates the presence of layer vacancies.

Kuma et al. (1994) studied a large collection of synthetic birnessite and buserite samples exchanged by monovalent (Na, K, Li, and Cs) and divalent (Ca, Mg, Sr, Be, and Ba) cations. Each species was studied by powder XRD and SAED. They found, in agreement with Post and Veblen (1990), that a, c, and β subcell parameters depend on the type of interlayer cation. They assumed that layer vacancies are associated with interlayer cations, which were found to be linearly arranged along the b axis. It was concluded that these vacancy-rich rows were separated by two complete rows of Mn octahedra. They emphasized that, in this respect, the structures of 7 Å-birnessite and 10 Å-buserite are notably different from chalcophanite.

The vacancy problem is closely related to the problem of the valence of Mn cations and to the determination of a correct crystal chemical formula for each birnessite modification. For example, the same chemical analysis of a birnessite sample can be interpreted either as $Na_{0.6}Mn^{4+}_{1.4}Mn^{3+}_{0.6}O_4$ or as $Na_{0.6}Mn^{4+}_{1.85}\square_{0.15}O_4$, where $\square$ stands for a lattice vacancy. In general, there might be different proportions of Mn^{4+}, Mn^{3+}, and Mn^{2+} cations, and there exists the possibility of replacing some O atoms by OH groups as well as some layer vacancies. For these reasons, no reliable technique exists to calculate the crystal-chemical formula of birnessite. The determination of the origin of superstructures observed in different birnessite species appears to be a prerequisite for determining their structural chemistry.
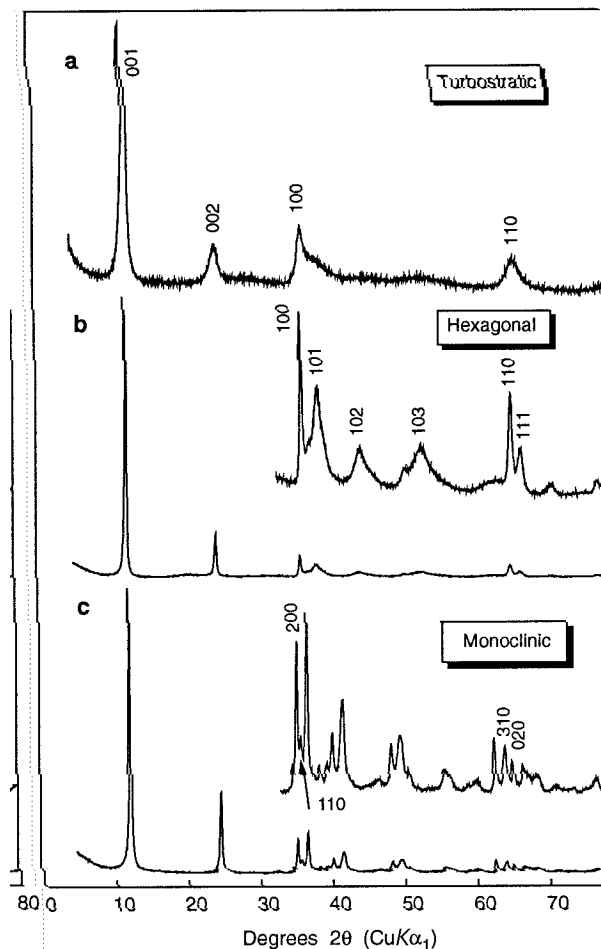
FIGURE 1. (**a**) X-ray diffraction pattern of natural Ca-rich birnessite with a turbostratic structure. (**b**) X-ray diffraction pattern of HBi (pH 3) showing the diagnostic reflections 102 and 103. (**c**) X-ray diffraction pattern of NaBi (pH 9) showing the diagnostic reflection pairs 200,110 and 310,020 that result from the departure of the hexagonal symmetry of the Mn layers.

Characteristic diffraction features of birnessite

Natural and synthetic birnessite samples may have turbostratic, one-layer hexagonal, and one-layer monoclinic structures.

The XRD patterns for birnessite with a turbostratic structure display 00l reflections and only two two-dimensional diffraction bands having 100 and 110 indices with $d_{100} \approx 2.42$ Å and $d_{110} \approx 1.42$ Å, respectively (Fig. 1a). XRD patterns for one-layer hexagonal birnessite contain, in addition to 00l and $hk0$ reflections, diagnostic 102 and 103 peaks with $d_{102} \approx 2.03$ Å and $d_{103} \approx 1.71$ Å (Fig. 1b). These reflections should have similar intensities if interlayer cations are located above or below the layer octahedral sites (Chukhrov et al. 1985).

The XRD patterns for one-layer birnessite with monoclinic subcells show 200, 110, and 310, 020 reflection pairs with d values equal to 2.52 ± 0.01, 2.48 ± 0.01, 1.445 ± 0.005, and 1.423 ± 0.005 Å, respectively (Fig.

1c). The presence of reflection pairs is induced by a strong distortion of the hexagonal symmetry of layers leading to an a/b ratio different from $\sqrt{3}$. As a result of this distortion $d_{310} > d_{020}$, whereas for an hexagonal sub-cell with the same b, c, and β values as in the monoclinic subcell, the condition of $b = a/\sqrt{3}$ leads to $d_{020} > d_{310}$.

EXPERIMENTAL METHOD

To determine the origin of superstructures, birnessite samples saturated with Na and Sr were studied. Na-rich buserite (NaBu) was prepared following the procedure of Giovanoli et al. (1970a). The solid phase was washed by centrifugation until the supernatant pH was approximately 9–10 (more than six times). The solid phase was initially characterized by XRD in a wet paste form, yielding the typical 10 Å layer spacing indicative of the NaBu phase. NaBi was obtained directly from the NaBu suspension by filtering and drying the solid at 40 °C. The low pH forms of birnessite were prepared at constant pH over a pH range of 2–5 from NaBu and then filtered and dried. Giovanoli et al. (1970b) and Silvester et al. (1997) show that the low pH forms of this mineral are Na^+ free and in the following discussion will be referred to by the general name HBi.

Sr-exchanged birnessite samples, hereafter referred to as SrBi, were prepared by shaking a NaBu suspension at 10 g/dm³ in 1 mol/dm³ $Sr(NO_3)_2$ solution for 24 h. The exchanged solid was then filtered and dried as for NaBi.

Powder XRD patterns were obtained using $CuK\alpha$ radiation with a Siemens D5000 powder diffractometer equipped with a Si(Li) solid-state detector. Intensities were measured at an interval of 0.05° 2θ and a counting time of 3 s per step. SAED patterns were recorded using a JEM 100c microscope equipped with a Kevex spectrometer and operated at 100 kV. Samples from dilute NaBu and Sr-exchanged buserite suspensions were suspended onto carbon grids, without previous drying or heating of the sample. The samples were subsequently mounted on a tilting sample holder. SAED patterns were interpreted as described by Drits (1987).

EXPERIMENTAL RESULTS

X-ray diffraction

The XRD pattern of our NaBi sample (Fig. 1c) is almost identical to that reported by Post and Veblen (1990). The measured d values correspond to a one-layer monoclinic subcell having parameters $a = 5.172$, $b = 2.849$, $c = 7.34$ Å, and $\beta = 103.3°$. XRD patterns of HBi samples (Fig. 1b) were all indexed with a one-layer hexagonal unit cell with $a = b = 2.848$, $c = 7.19$ Å, and $\gamma = 120°$. The $10l$ reflections are broadened because of the presence of stacking faults in microcrystals.

Selected-area election diffraction

NaBi. Figures 2a and 2b show the two main types of SAED patterns observed for NaBi microcrystals (birnessite type I and II, respectively). Both patterns contain a set of strong $hk0$ reflections distributed according to a
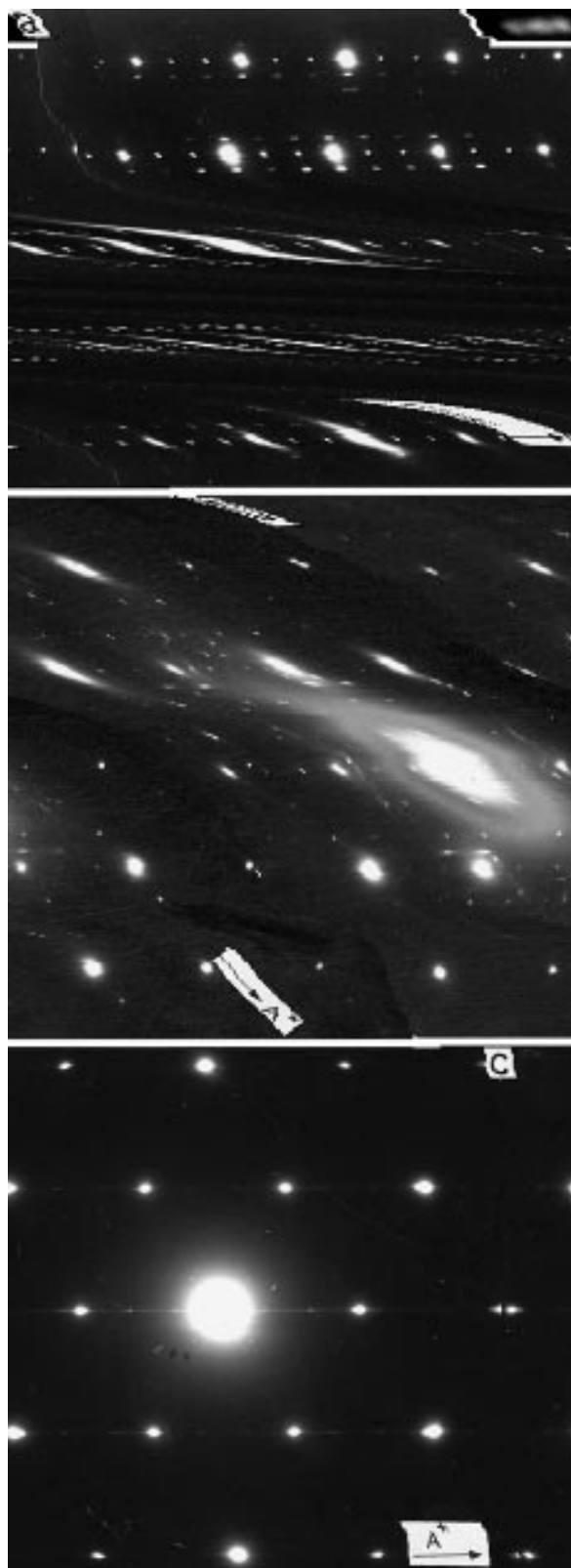

FIGURE 2. Selected-area electron diffraction patterns for NaBi (**a** and **b**) and HBi (**c**) microcrystals. Upper right insert of SAED pattern (**a**) shows the triplet of satellites.
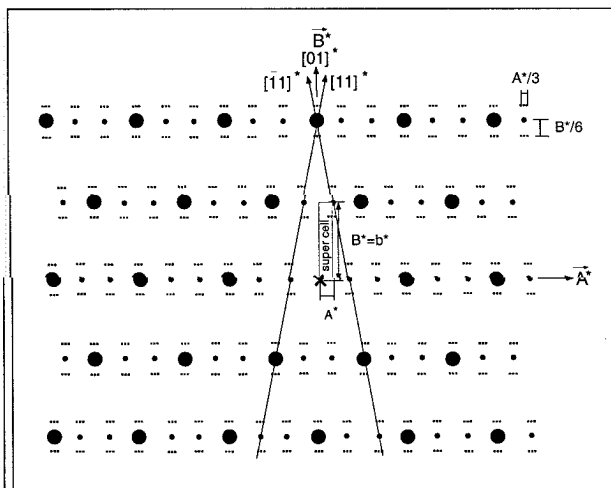
FIGURE 3. Idealized distribution of diffraction maxima observed in the SAED pattern of Figure 2a. Large and medium solid circles correspond to subcell and supercell reflections, respectively. Small black points correspond to satellites. A^* and B^* are the supercell parameters.

FIGURE 4. Idealized distribution of diffraction maxima observed in the SAED pattern of Figure 2b. Large and medium solid circles correspond to subcell and supercell reflections, respectively. Open circles and small black ellipsoids elongated along $[1\bar{1}]^*$ and $[11]^*$ are satellites. A^* and B^* are the supercell parameters. In all patterns, the A^* axis is oriented horizontally.

pseudo-hexagonal symmetry and corresponding to the layer subcell determined by XRD. According to the SAED observations, the proportion of birnessite type II is much higher.

NaBi type I. The distribution of reflections in the SAED pattern of NaBi type I (Fig. 3) may be described by a centered layer supercell with parameters $A = 3a = 15.52$ Å, $B = b = 2.85$ Å, and $\gamma = 90°$. Each of the subcell and supercell reflections is surrounded by six satellites with one pair along $[01]^*$ at $\pm b^*/6$, and two other pairs located along $[\bar{1}1]^*$ and $[11]^*$, respectively. The distance between a central $hk0$ reflection and any one of these four satellites is

$$[(A^*)^2 + (B^*)^2]^{1/2}/6 = 1/6d_{110}.$$

Thus, only a cell with $A_S^* = A^*/6$ and $B_S^* = B^*/6$ may account for the positions of all diffraction maxima, including the satellites; this cell will be referred to as the S cell. The intensity of satellites depends on the value of k (see Fig. 2a). In particular the satellites around $h00$ reflections have equal intensities. Satellites around reflections with $k \neq 0$ have different intensities: Inner satellites with $k - \frac{1}{6}$ are more intense than outer satellites with $k + \frac{1}{6}$. The difference between the intensities of inner and outer satellites increases with increasing k values (Fig. 2a).

NaBi type II. Another type of SAED pattern observed for NaBi microcrystals is shown schematically in Figure 4 (cf. Fig. 2b). Two sorts of satellites may be distinguished. The distribution of superreflections corresponds to a base-centered supercell with $A = 3a = 15.52$ Å, $B = 3b = 8.55$ Å, and $\gamma = 90°$. The satellites of the first type (open circles) are near some hk reflections at $B^*/2 = \pm b^*/6$ along $[01]^*$. These satellites have the coordi-
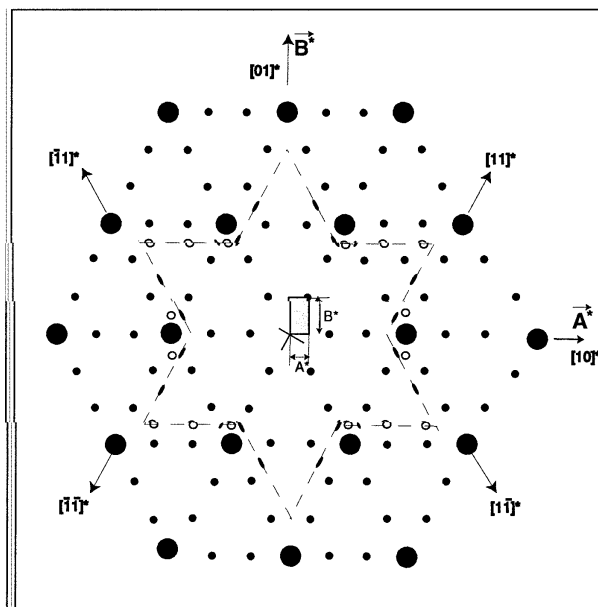
nates $h,k \pm \frac{1}{2}$. As above, the satellite intensity depends on the value of k.

The distribution of the second type of satellite resembles an incomplete six-pointed star (Figs. 2b and 4). The satellites are elongated along different directions, which are rotated by 60°. The distance between these satellites and their nearest subcell or supercell reflection is $\frac{1}{2}/[(A^*)^2 + (B^*)^2]^{1/2}$ Satellites elongated along $[1\bar{1}]^*$ are placed in the middle of two nearest main reflections located along $[11]^*$. There are no satellites along the $[10]^*$ direction. Thus an S cell with parameters $A_S^* = A^*/2 = a^*/6$ and $B_S^* = B^*/2 = b^*/6$ is necessary to describe the positions of all diffraction maxima, including satellites.

HBi. Figure 2c shows an SAED pattern typical for HBi. The reflections are distributed according to the expected hexagonal symmetry with layer hexagonal cell parameters of $a = 2.84$ Å or base-centered cell parameters of $a = 4.927$, $b = 2.84$ Å, and $\gamma = 90°$. Such SAED patterns have been observed previously for natural and synthetic one-layer hexagonal birnessite (Giovanoli et al. 1970b; Chukhrov et al. 1978, 1989). However, the SAED patterns shown in Figure 2c contain extremely weak but noticeable additional reflections distributed according to the base-centered supercell with $A = 3a = 14.78$ Å, $B = 2.845$ Å, and $\gamma = 90°$.

SrBi type I. Three different SAED patterns were identified for SrBi microcrystals (Fig. 5). Figure 6 reproduces schematically the position and shape of diffraction maxima observed in SAED patterns of the first type (Fig. 5a). A supercell can be identified with the parameters $A^* =$
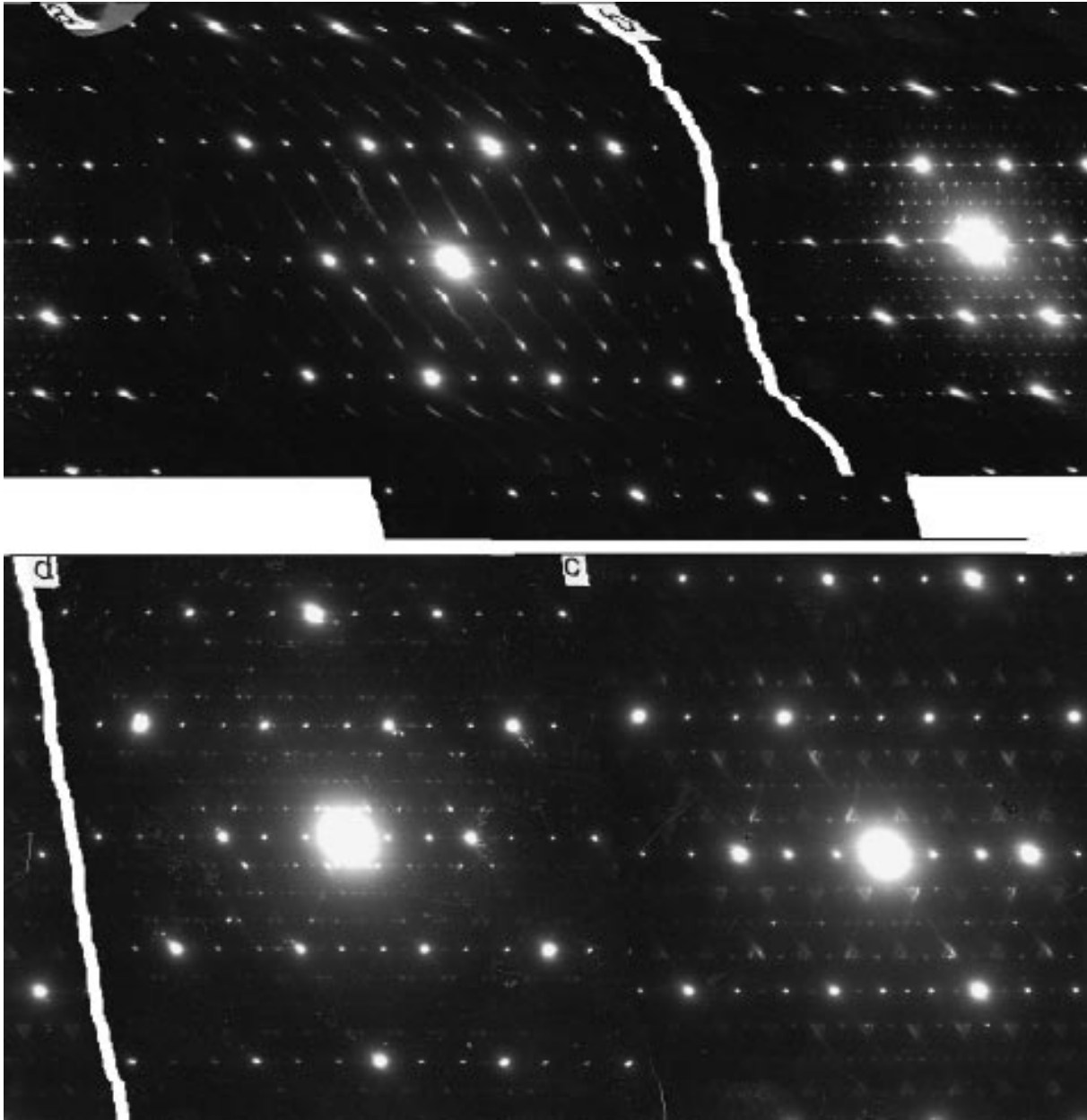
FIGURE 5. Main types of SAED patterns observed for SrBi microcrystals. The various microcrystals differ from each other by their super-cells. (**a**) SrBi type I, (**b**) SrBi type II. (**c**) and (**d**) SrBi type III.

$a^*/3$, $B^* = b^*$, and $\gamma^* = 90°$. One can note that each hk reflection is surrounded by a pair of diffraction maxima strongly elongated in the $[\bar{3}1]^*$ direction. Each hk reflection is also surrounded in the direction parallel to $[11.1]^*$, almost perpendicular to $[\bar{3}1]^*$, by a pair of these elongated maxima. The positions of the main spots and elongated maxima can be described by a periodic two-dimensional network. The cell of this network has the parameters $A_S^* = \frac{1}{7}(11A^*+B^*)$ and $B_S^* = \frac{1}{7}(-3A^*+B^*)$ oriented along the supercell directions $[11.1]^*$ and $[\bar{3}1]^*$, respectively.

One can note (Fig. 6) the regular distribution of the diffuse (elongated) maxima relative to the main reflections: One pair of these maxima are placed along the B_S^* axis at distances of $\pm 2B_S^*$ and the other pair along the A_S^* axis at distances of $\pm 2A_S^*$. Such mutual arrangement of main and diffuse reflections leads to specific values of the h_s and k_s indices. In particular $h_s + k_s = 7n$ ($n = 0$, 1, 2, . . .) for the main reflections and $h_s + k_s = 2, 5, 9,$ 13. . . for the diffuse maxima. The nodes corresponding to $h_s + k_s = 1, 3, 4, 6, 8. . . .$ have zero intensity.

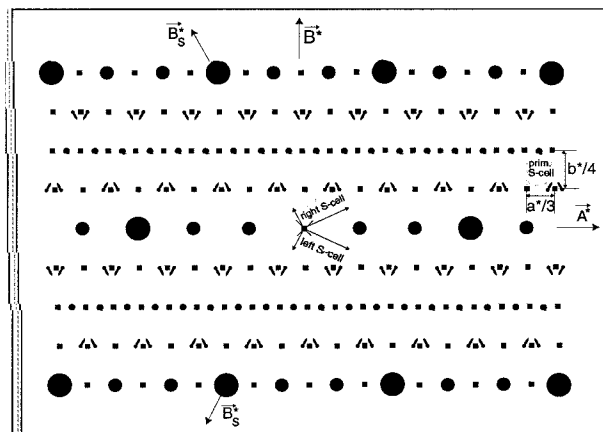**SrBi type II and III.** The second type of SAED pat-
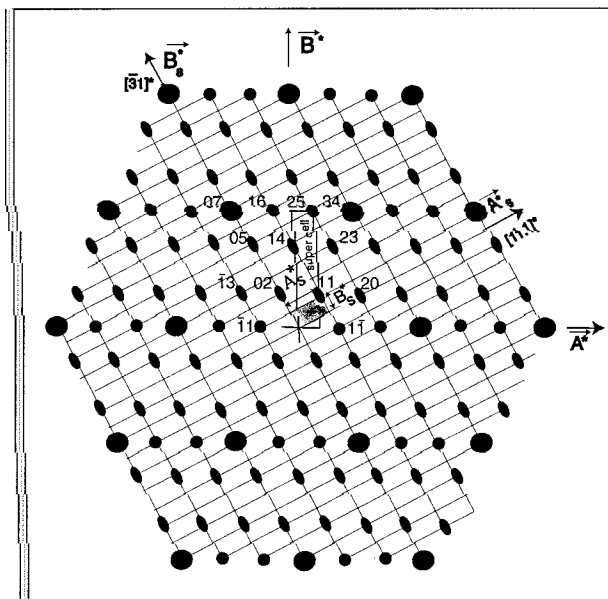
FIGURE 6. Idealized distribution of diffraction maxima observed in the SAED pattern of Figure 5a. Large and medium solid circles correspond to subcell and supercell reflections, respectively. Black ellipsoids elongated along $[\bar{3}1]^*$ are satellites. A^*, B^* and A_s^*, B_s^* are the supercell and S* cell parameters, respectively.

terns (Fig. 5b) corresponding to SrBi microcrystals contains a reflection network that can be described by a rectangular primitive cell with $A_{or}^* = a^*/3$ and $B_{or}^* = b^*/4$. Note that among $h00$ reflections, those with $h = 2n + 1$ are absent. The SAED patterns shown in Figures 5c and 7 are a superposition of three reflection networks, corresponding to at least two separate structural varieties. The first reflection network (small black squares) is rectangular and is identical to that shown in Figure 5b. The second diffraction pattern, which can be extracted from Figure 7, is illustrated schematically in Figure 8. The positions of these points can be described by a two-dimensional network with the cell parameters $A_s^* = \frac{1}{8}(13A^* + B^*)$ and $B_s^* = \frac{1}{8}(-3A^* + B^*)$. Here A^* and B^* are the conventional super-cell parameters. Relative to this supercell A_s^* and B_s^* are oriented along $[13.1]^*$ and $[\bar{3}1]^*$ directions, respectively (Fig. 8). As in the previous case each reflection of the subcell and supercell is surrounded by four diffuse maxima elongated in the $[\bar{3}1]^*$ direction. Two are located along the $[13.1]^*$ direction at $\pm 2A_s^*$ from any reflection, whereas the other two are located along the $[\bar{3}1]^*$ direction at $\pm 2B_s^*$ from the same reflection.

Because the $h_s + k_s$ values for all diffraction maxima are even, the corresponding S cell in real space is characterized by a base-centered cell. However, the values of $h_s + k_s$ depend on the type of reflection (Fig. 8).

The remaining reflections of Figure 7 (third reflection network) may be generated by a 180° rotation of the second network around the $[10]^*$ axis. Thus the schematic SAED pattern shown in Figure 7 is the superposition of
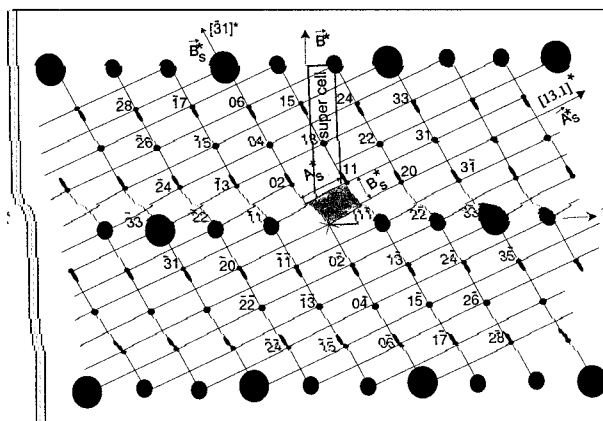

FIGURE 7. Idealized distribution of diffraction maxima observed in the SAED pattern of Figure 5c. Large and medium solid circles correspond to subcell and supercell reflections, respectively. The small squares correspond to reflections observed in the SAED pattern shown in Figure 5b. The other reflections are connected by a mirror plane and correspond to a second structural component, which is twinned. S* cells are shown for each twin.

diffraction patterns from crystallites having a rectangular cell and two other crystallites having twinned S cells. The main difference between the SAED patterns for SrBi microcrystals in Figures 5c and 5d (SrBi type III) is that the diffuse streaks of Figure 5c are transformed into normal sharp and intense reflections in Figure 5d.

INTERPRETATION

Structure of the interlayer

NaBi. We assume that the superreflections in the SAED patterns originate from an ordered distribution of interlayer cations and H_2O molecules. This arrangement must reflect the total layer charge and ordering of negative charges within layers. The validity of these assumptions is discussed below. In NaBi, surface O atoms and

FIGURE 8. Distribution of diffraction maxima corresponding to one of the twinned structures observed in Figure 7.
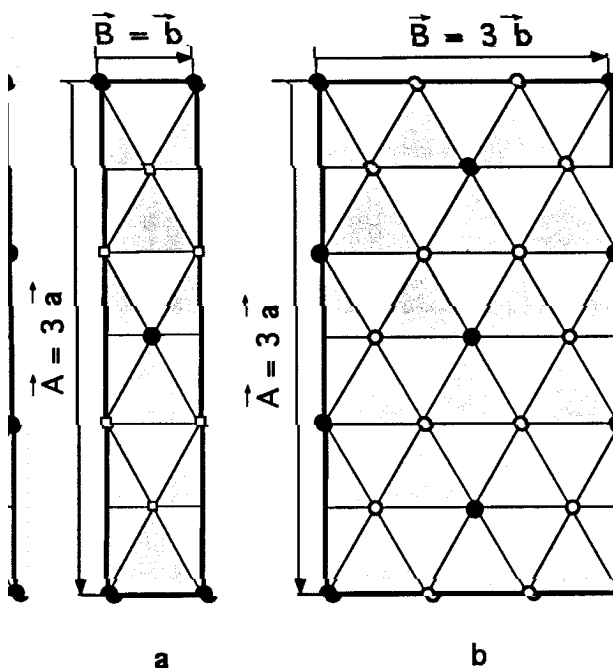
FIGURE 9. Supercells for NaBi types I and II with $A = 3a$ and $B = b$ (**a**), and $A = 3a$ and $B = 3b$ (**b**). In the first cell, solid circles and open squares correspond to interlayer sites with different Na occupancies. In the second cell, solid and open circles correspond to Na and H_2O positions, respectively.

sites occupied by interlayer Na and H_2O molecules are very close in projection in the *a-b* plane (Post and Veblen 1990).

NaBi type I. The interlayer supercell with $A = 3a = 15.52$ Å and $B = b = 2.85$ Å is represented in Figure 9a. Among the six available sites for Na and H_2O within the interlayer supercell the two sites with coordinates 0,0 and ½,½ must have a higher scattering power because the cell is base-centered. According to the chemical analysis (Silvester et al. 1997) each octahedral site has 0.30 Na atoms associated with it. This means that the supercell interlayer contains 1.8 Na atoms. If Na atoms were at supercell nodes 0,0 and ½,½ with 0.9 probability, then Na-Na pairs would be aligned along the *b* axis, which is not acceptable because Na must alternate with H_2O molecules. As a consequence, it is necessary to assume that all six supercell sites are occupied by either Na or H_2O, but the probability of Na occupancy at 0,0 and ½,½ must be higher.

NaBi type II. Another distribution of Na and H_2O molecules, which avoids neighboring Na cations, is present in NaBi type II. The supercell ($A = 3a = 15.51$ Å, $B = 3b = 8.55$ Å) contains 18 sites available for Na and H_2O (Fig. 9b). It is easy to see that the 5.4 (18×0.3) atoms of Na can now be readily distributed in such a way that each Na is surrounded by six H_2O molecules. Thus this supercell contains 6 sites for Na and 12 sites for H_2O molecules. In the case of a homogeneous distribution of Na atoms, each of the six Na sites should be occupied

with a probability of 0.9 ($0.9 \times 6 = 5.4$). However, because of the base-centered distribution of interlayer Na, it seems reasonable to assume that the 0,0 and ½,½ positions have a higher occupancy probability. If Na atoms occupy all available sites with 100% probability, the maximum possible content of Na atoms per layer octahedron is 0.33.

HBi. According to previous XRD data (Chukhrov et al. 1985) birnessite layers contain many vacancies. The very weak superreflections observed in the SAED patterns can be interpreted as resulting from a random or almost random distribution of layer vacancies. But this interpretation may be misleading. Indeed, if interlayer Mn cations are placed just above or below vacancies, then in projection in the *a-b* plane vacant sites will have the same scattering power as filled layer sites. In this case the distribution of *hk*0 reflections would not be sensitive to the possible order-disorder of vacancy distribution. If interlayer Mn cations are placed above and below vacancies the scattering power of vacant sites would be enhanced and the absence of *hk*0 superreflections would indicate a random distribution of vacancies. Silvester et al. (1997) show that interlayer Mn cations are located either above or below the layer vacancies, which is consistent with the weakness of superreflections for HBi. These superreflections arise from the regular distribution of interlayer $Mn^{2+/3+}$ and the associated interlayer H_2O molecules, each cation being octahedrally coordinated to three layer O atoms and to three interlayer H_2O molecules. The superreflections in the SAED patterns reflect the tendency toward an ordered distribution of vacancies and the associated interlayer $Mn^{2+/3+}$ and H_2O molecules, over the nodes of the base-centered cell with $A = 3a = 3\sqrt{3}b$ and $B = b = 2.845$ Å.

SrBi type I. The supercell observed in the SAED pattern of Figure 5a with $A = 15.59$ and $B = 2.83$ Å is analogous to that determined for NaBi type I. For charge-balance reasons we assume that 0.15 Sr atom per octahedral site exists. The interlayer super-cell must then contain 0.9 cations. Because of the high scattering power of Sr, the base-centered cell, and the low Sr interlayer content, there is no doubt that Sr occupies 0,0 and ½,½ sites rather than the other four supercell positions. As for NaBi, Sr atoms cannot occupy two successive sites along [01].

SrBi type II and III. Rectangular networks of reflections observed for SrBi can be described by a supercell with $A = 3a = 15.60$ Å and $B = 4b = 11.32$ Å (Fig. 10). There are 24 available sites and the cell contains 3.6 Sr atoms. The cell would therefore contain four sites with 90% probability of occupancy. A possible model for the distribution of interlayer Sr is represented in Figure 10. Note that the periodicity of the projection of Sr and H_2O along the *A* axis is $A/2$. For this reason *h*00 reflections have $h = 2n$ (Fig. 5b and 5c). Unit cells for the structural components responsible for the other reflections observed in Figures 5c and 5d are considered in the next section.
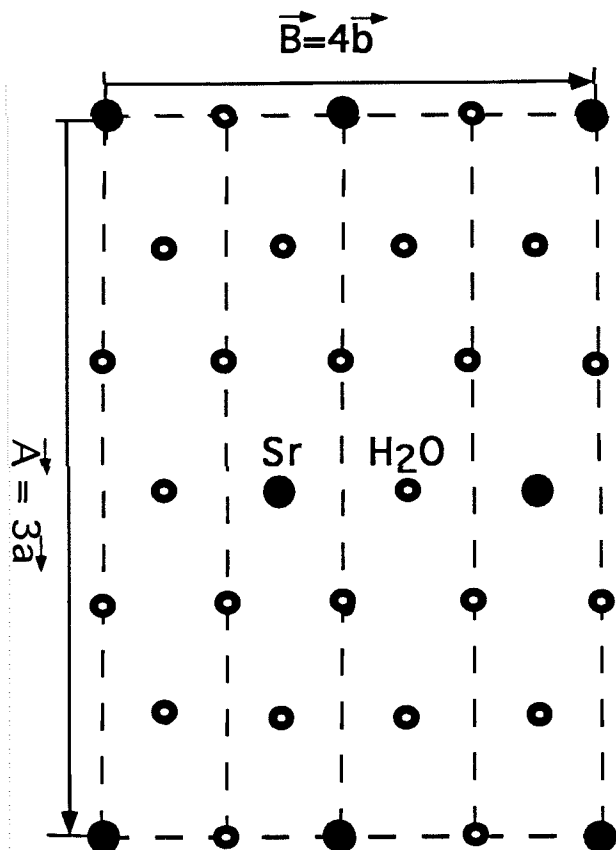
FIGURE 10. A model for the interlayer distribution of Sr (large solid circles) and H_2O molecules (small open circles) in SrBi microcrystals with supercell parameters $A = 3a$ and $B = 4b$.

The origin of satellites for Na-rich birnessite

Wilson (1964) showed that if each *hkl* node of the reciprocal lattice is surrounded by two satellites at $\pm\lambda$ from the node along the $b*$ axis and the outer pair is weaker than the inner pair, then the crystal contains a modulation along the b axis with a periodicity λ. In addition, the structure amplitude will be higher for higher d_{010} values.

NaBi type I. The theoretical considerations developed by Wilson (1964) are used to interpret qualitatively some SAED features observed in Figure 2a. In Figure 11, Na and H_2O are located in such a way that d_{010} values change periodically from $d_1 = d_{010} + \delta$ to $d_3 = d_{010} - \delta$ with $\lambda = 6b = 17.1$ Å. In the model it is considered that the relative scattering power of atoms located in planes parallel to (010) decreases with decreasing interplanar distances from 1.0 to 0.7 with a 0.05 step. Using the atomic positions of Figure 11, structure factors of superreflections and satellites were calculated by assuming that the relative positions of these planes, or the y/B_s coordinates for Na and H_2O molecules along the B_s axis for half the period, are equal to, 0.0, 0.087, 0.172, 0.257, 0.34, 0.421, and 0.50 ($A_s = 3a = 15.51$ Å; $B_s = 6b = 17.1$ Å). Accordingly, d values between two nearest planes vary be-
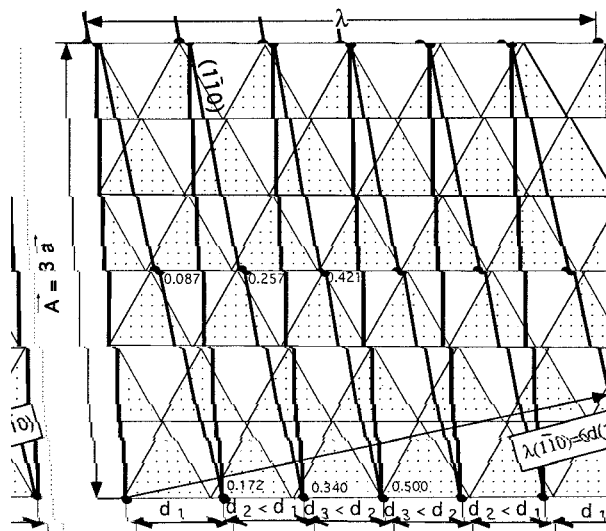

FIGURE 11. Idealized structural model for NaBi interlayers of the first type. Regular white and dotted triangles correspond to the O atom layer. The solid circles represent sites enriched with Na. The vertical thick lines with variable distance correspond to (010) planes, which contain Na sites. Oblique lines with variable distances correspond to (110) planes.

tween 1.488 and 1.351 Å, whereas in the strictly periodic structure this interplanar distance should be equal to 1.425 Å ($b/2$). As noted in the previous section, the x coordinates for Na and H_2O correspond to their ideal values. Using this model significant diffraction intensities were obtained only for nodes corresponding to the main reflections and for satellites located at distances of $\pm b*/6$. Additionally, this model led to greater intensity for inner satellites relative to outer satellites, as observed experimentally (Figs. 2a and 3). This model also accounts for the presence of satellite pairs along $[11]*$ and $[1\bar{1}]*$ directions near each hk reflection at distances of $r*/6$, where $r* = [(A*)^2 + (B*)^2]^{1/2}$ (Figs. 2a and 3). As seen in Figure 11 the (110) and ($1\bar{1}0$) planes also contain Na and H_2O molecules and their interplanar distances are also modulated along their normal. This periodic variation results from the fact that the displacement of Na and H_2O along the b axis can be decomposed into two components parallel and perpendicular to (110, $1\bar{1}0$) planes. As can be seen in Figure 11 the wavelength of the variation of the $d_{110,1\bar{1}0}$ values is equal to $\lambda_{110,1\bar{1}0}$ $6d_{110,1\bar{1}0}$.

NaBi type II. The same interpretation applies to satellites of Figures 2b and 4. The directions of displacements for Na and H_2O within the S cell ($A_s = A = 3a$, $B_s = \lambda = 2B = 6b$) are shown in Figure 12. Calculations with the relative scattering power of planes decreasing (from 1.0 to 0.7) with decreasing d values explains qualitatively both the origin of satellites at distances of $k \pm$ ½ from hk reflections and the different intensities of inner and outer satellites.

The second type of satellites are a direct consequence of the specific distribution of Na and H_2O within the su-

FIGURE 13. A model of the mutual arrangement of Sr (large solid circles) and H_2O molecules (small solid circles) in the interlayers of SrBi microcrystals that are characterized by the SAED pattern of Figure 5a. The probability of Sr occupancy is about 0.4–0.45. Arrows show the directions of Sr displacements from their ideal positions. A,B and A_s,B_s are the parameters for the supercell and S cell, respectively. λ_1 and λ_2 are the wavelengths describing the periodicity of the $d_{\bar{3}10}$.
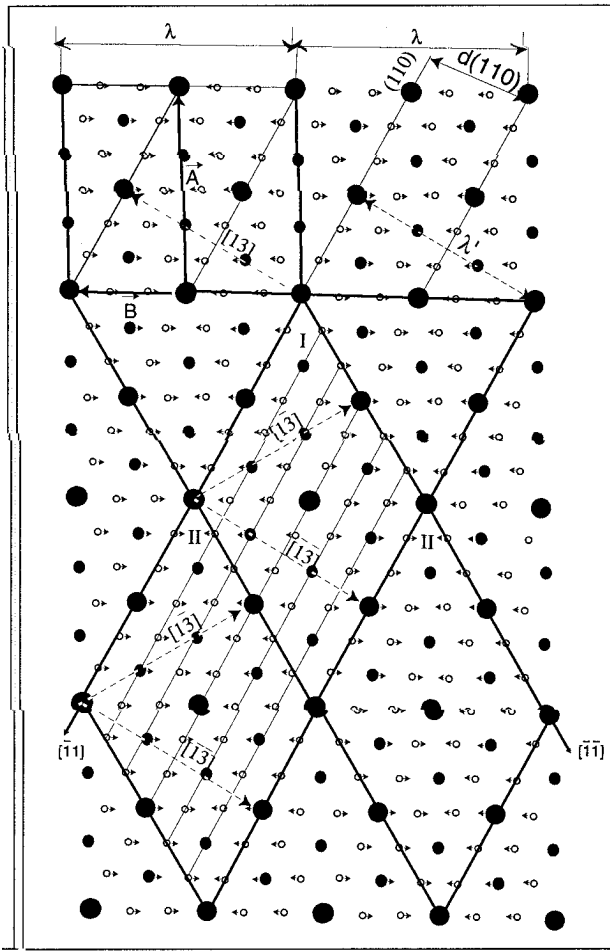
FIGURE 12. Idealized structural model for NaBi interlayers of the second type. Large and small circles represent Na sites with different degrees of occupancy. Small open circles correspond to H_2O sites. Arrows attached to circles indicate the periodic displacement of interlayer species along the B axis. In the upper left portion of the diagram two supercells with $A = 3a$ and $B = 3b$ are shown. Unit cells I and II in the form of a rhomb have the same sizes and shapes but differ slightly in the arrangement of Na and H_2O sites. λ and λ' are wavelengths of variation of interplanar distances for (010) and (110), respectively.

As noted previously, some of these satellites are elongated along the $[11]^*$ or $[1\bar{1}]^*$ directions (Fig. 4). To understand the origin of this feature two adjacent rhomb-shaped unit cells (I and II) were chosen to have sides parallel to $[\bar{1}1]$ and $[\bar{1}1]$ and edge lengths of $(A^2 + B^2)^{1/2}$ (Fig. 12). These cells (I and II) have the same size but differ slightly in their atomic positions. Because of this peculiar atomic arrangement, planes parallel to (110) and located in two neighboring type I and II unit cells do not scatter strictly in phase because Na and H_2O located in the same plane are shifted in opposite directions (Fig. 12). The perturbation of the wave phases leads to the elongation of satellites in the $[1\bar{1}]^*$ direction. The same effect occurs for planes parallel to $(1\bar{1}0)$ leading to the formation of satellites elongated along $[11]^*$. Note that the absence of satellites along the $[10]^*$ direction is explained by the fact that the ($h00$) planes are always parallel and have a uniform spacing.

The origin of satellites for Sr-exchanged birnessite

SrBi type I. Figure 13 shows the relationship between the supercell with $A = 3a$, $B = b$, and $\gamma = 90°$ and the S cell with $A_s = \frac{1}{2}(A + 3B)$ and $B_s = \frac{1}{2}(11B - A)$. As can be seen in Figure 13 the S-cell contains seven sites occupied by Sr with a probability equal to 0.45–0.40 so that each Sr is surrounded by six nearest H_2O molecules. As for NaBi microcrystals, satellites in the SAED patterns of SrBi are associated with the periodic displacement of Sr cations around their ideal positions. The simplest model that would explain the observed effects is one in which Sr cations are shifted periodically along the normal to $(\bar{3}10)$ planes. Such a displacement leads to a periodic variation of $d_{\bar{3}10}$. As

percell with $A = 3a$ and $B = 3b$ and of their periodic displacements along the b axis. As shown in Figure 12, planes parallel to $(110,1\bar{1}0)$ pass through Na and H_2O sites. The distance between these planes varies periodically along the $[\bar{1}3]$ and $[1\bar{3}]$ directions because of the periodic displacement of Na and H_2O along the b axis. The periodicity of wavelengths (λ') is equal to $2d_{110,1\bar{1}0}$, and in the reciprocal lattice each reflection is surrounded by a pair of satellites located along $[11]^*$ and $[1\bar{1}]^*$ with relative coordinates $h \pm \frac{1}{2}$ and $k \pm \frac{1}{2}$. Due to the synchronized variation of the interplanar distances and of their scattering powers, an asymmetrical distribution of intensity for inner and outer satellites is obtained and is observed experimentally (Fig. 2b).
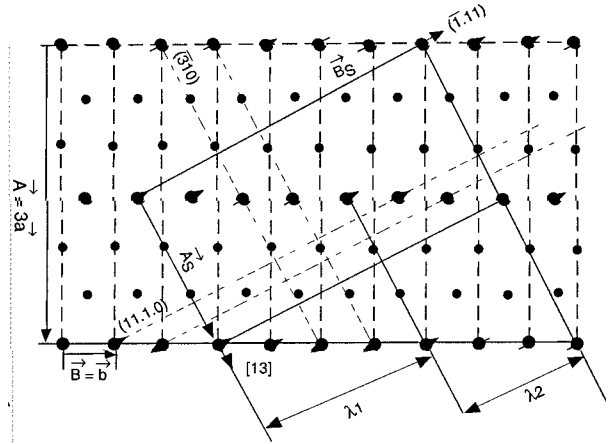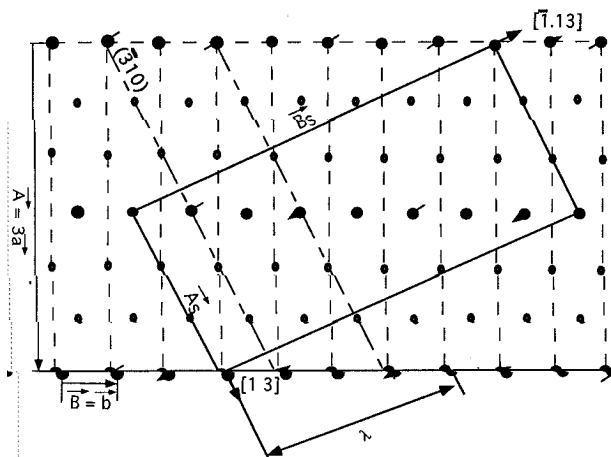
FIGURE 14. A model of the mutual arrangement of Sr (large solid circles) and H_2O molecules (small solid circle) in the interlayers of SrBi microcrystals that are characterized by the SAED pattern shown in Figure 5c. The probability of Sr occupancy is about 0.4–0.45. The arrows show the directions of Sr cation displacement in correspondence with the periodic variation of $d_{\overline{3}10}$. A,B and A_s,B_s are the parameters of the supercell and S cell, respectively.

seen in Figure 13 the S cell contains seven $(\overline{3}10)$ planes passing through Sr cations. If the values of $d_{\overline{3}10}$ vary with $\lambda = [7d_{\overline{3}10}]/2$ then each main reflection is surrounded by two satellites at distances of $2 B_S^* = 2/[7d_{\overline{3}10}]$ along the $[\overline{3}1]^*$ direction, as observed in the SAED pattern. This model also accounts for the zero intensity of nodes with $h_s + k_s = \pm1, \pm3, \pm4,\ldots$ as well as the presence of satellites at distances of $2A_S^*$ from hk reflections along $[11.1]^*$. It also provides an explanation of the origin of diffuse and elongated sat-
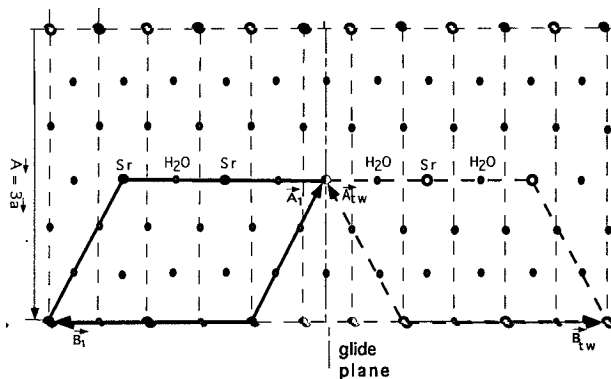

FIGURE 15. Mutual arrangements of Sr and H_2O in the two oblique cells of twins. Large solid circles correspond to sites occupied by Sr in the twin components with A_1 and B_1 parameters. Large open circles correspond to Sr sites in the other twin component with A_{tw} and B_{tw} parameters. Small open circles correspond to H_2O molecules.

ellites (Figs. 5a and 6). As mentioned previously, the S cell contains an odd number of $(\overline{3}10)$ planes passing through Sr sites. For this reason it is impossible to have an oscillation of $d_{\overline{3}10}$ with a period exactly equal to $[7d_{\overline{3}10}]/2$. In the simplest case two periods may take place with $\lambda_1 = [4d_{\overline{3}10}]/7$ and $\lambda_2 = [3d_{\overline{3}10}]/7$ (Fig. 13). A random alternation of these two periods with an average periodicity of $[7d_{\overline{3}10}]/2$ results in elongated diffuse satellites at distances of $\pm2B_S^*$ from hk reflections. A complete treatment of this structural model would undoubtedly give continuous streaks instead of the sharp maxima observed experimentally.

SrBi type II and III. Figure 14 shows the S cell with $A_s = \frac{1}{2}(A + 3B)$ and $B_s = \frac{1}{2}(13B - A)$ corresponding to the diffraction data shown in Figure 8. This cell contains eight sites for Sr and eight $(\overline{3}10)$ planes passing through Sr cations. Again, we can assume that Sr cations are shifted in the direction normal to $(\overline{3}10)$ planes in such a way that $d_{\overline{3}10}$ values vary with the wavelength $\lambda = [8d_{\overline{3}10}]/2$ because the satellites in Figure 8 are placed along the $[\overline{3}1]^*$ direction at distances of $\pm2B_S^*$. Taking into account that the S cell is base centered and contains an even number of $(\overline{3}10)$ planes containing Sr, a model for the displacement of Sr within the S cell, with $\lambda = 4d_{\overline{3}10}$ can be proposed (Fig. 14). This model explains the presence of satellite pairs at distances of $\pm2A_S^*$ from hk reflections along $[13.1]^*$. The diffuse character of the satellites and their elongation in the $[\overline{3}1]^*$ direction are induced by the variable values of Sr displacement throughout the crystal. Consequently, an irregular fluctuation of λ occurs in the crystal and again elongated streaks are observed, instead of sharp reflections. As mentioned previously, the reflections with $h_s + k_s = \pm4, \pm12$ are very weak but sharp because Sr cations shifted from their ideal sites (Fig. 14) give zero contribution to the intensity for these reflections.

Finally, consider SAED patterns for the third type of SrBi microcrystal, which contains only sharp reflections (Fig. 5d). Diffuse and elongated maxima of Figure 5c are transformed into normal point reflections in Figure 5d. It is likely that the probability of the Sr site occupancy is now the same for all supercells of each twin. Figure 15 shows the relationship between the supercell with $A = 3a = 15.59$ Å and $B = b = 2.83$ Å and the two twinned oblique supercells with $A = \frac{3}{2}(a^2 + b^2)^{1/2} = 8.87$ Å, $B = 4b = 11.32$ Å, and $\gamma = 118.7°$.

The corresponding reciprocal unit cell $[A_S^* = \frac{1}{8}(13A^* + B^*)$ and $B_S^* = \frac{1}{8}(B^* - 3A^*)]$ agrees with the reflection positions observed experimentally (Fig. 5d). There are 12 available sites and the supercell contains 1.8 Sr cations. The cell would therefore contain two sites with a site occupancy probability of 90%. A possible model for the distribution of Sr is represented in Figure 15. In each twin, Sr is surrounded by six H_2O molecules and the periodicity of the projection of Sr along the A axis is $A/2$. This position of Sr atoms is almost certainly determined by the ordered distribution of Mn^{4+} and Mn^{3+} atoms in adjacent birnessite layers as discussed below.

DISCUSSION

Origin of the layer charge

The analysis of satellites for Na-rich and Sr-exchanged birnessite microcrystals indicates a dynamic fluctuation of the positions of scattering atoms. This displacement can be achieved very easily in the interlayer space because of the great mobility of the interlayer species in response to layer charge distribution. In addition, the variety of diffraction effects observed for NaBi and SrBi, all having very similar layer structure and cation compositions, can hardly be explained by different layer vacancy distributions. Thus we can infer that the main source of negative layer charge is the presence of Mn^{3+} cations, rather than vacancies. The presence of a considerable amount of Mn^{3+} in the layer of NaBi is supported by other considerations. One explanation for the distortion from the hexagonal symmetry of the layer, demonstrated by the deviation of the a/b ratio from $\sqrt{3}$, is the presence of Mn^{3+} cations and the consequent Jahn-Teller distortion. One could assume that the long bonds of the distorted octahedra are oriented along the a axis of the monoclinic subcell, leading to a relative lengthening of the a parameter in comparison with b. In the layer structure of crednerite (Töpfer et al. 1995) the layers contain only Mn^{3+} and the unit cell is characterized by $a = 5.578$, $b = 2.881$ Å; $a/b = 1.936$. A comparison of these values with those for NaBi ($a = 5.175$ and $b = 2.847$ Å; $a/b = 1.818$) shows that whereas the b parameter has a low sensitivity to the presence of Mn^{3+}, the a parameter has a very high sensitivity. If we assume that $a = b\sqrt{3} = 4.93$ Å for a pure Mn^{4+} layer and that there is a linear relation between the Mn^{3+}/Mn^{4+} ratio and the elongation of the a parameter, then the fraction of Mn^{3+} in NaBi layers would be 0.38. This very crude calculation is consistent with the measured exchange capacity (Silvester et al. 1997) and seems a reasonable explanation of the layer distortion.

However, as discussed below, the replacement of one type of interlayer cation by another may be accompanied by the appearance of layer vacancies. For example, Mg cations in MgBi occupy sites above or below layer cation sites (Post and Veblen 1990). If these layer sites were occupied by Mn cations then a strong electrostatic repulsion would exist. These layer sites must therefore be vacant to provide an energetically favorable O triangle for Mg adsorption. Furthermore, it is difficult to believe that the decrease of the a parameter from NaBu (5.23 Å) to NaBi (5.16 Å) and from Mg-exchanged buserite (5.173 Å) to MgBi (4.94 Å) described by Kuma et al. (1994) is due only to the interlayer structure modification. A similar decrease of the a parameter has been described for the Mg-for-Na exchange in birnessite both by Post and Veblen (1990; from 5.175 to 5.05 Å) and by Kuma et al. (1994; from 5.16 to 4.94 Å). The a parameter of Be-exchanged birnessite (4.915 Å) is such that the a/b ratio equals the $\sqrt{3}$ ratio corresponding to ideal hexagonal symmetry. Such strong variations of the a parameter are
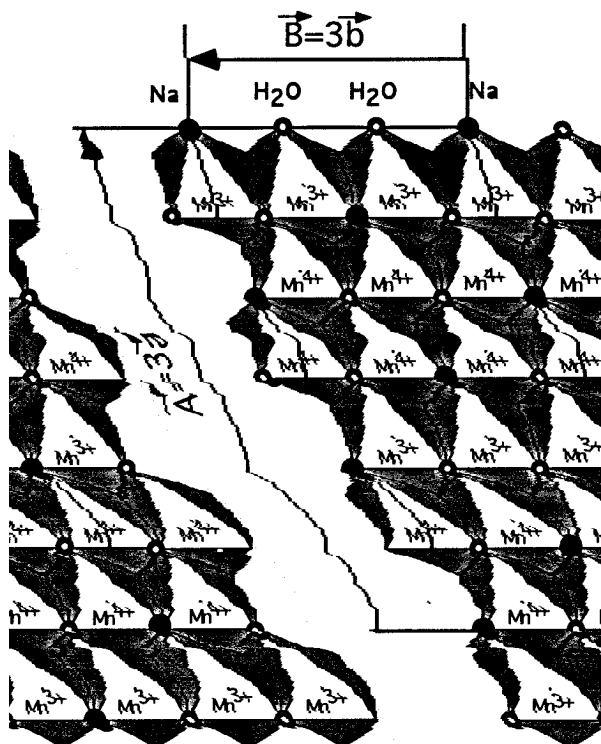

FIGURE 16. Ordered arrangement of Mn^{3+} and Mn^{4+} cations among available octahedral sites. A supercell with $A = 3a$ and $B = 3b$ and an ordered distribution of Na (solid circles) and H_2O (open circles) is shown.

more likely due to changes in the composition of layer cations, in particular the Mn^{3+}/Mn^{4+} ratio, a high a value indicating a high proportion of Mn^{3+}. In agreement with this assumption, the dehydration of 10 Å NaBu and the substitution of Mg or Be for Na would be accompanied either by the oxidation of Mn^{3+} or the disproportionation of Mn^{3+} to Mn^{2+} and Mn^{4+} and the concomitant formation of layer vacancies (Silvester et al. 1997).

Cation ordering in Mn layers

An interesting question is how Mn^{3+} is distributed in the layers. Because of the Jahn-Teller distortion, a random distribution of Mn^{3+} and Mn^{4+} among available sites combined with a random azimuthal orientation of Mn^{3+} octahedra would lead to unfavorable steric strains. The simplest way to avoid layer strains is the distribution of Mn^{3+} in rows parallel to b and the orientation of the long Mn^{3+}-O bonds along the a axis and, as a consequence, to assume that Mn^{3+} cations tend to order. Then, each Mn^{3+} would share two edges parallel to (010) with nearest Mn^{3+} octahedra and four edges parallel to (310) and ($3\bar{1}0$) planes with Mn^{4+} octahedra (Fig. 16). In addition, such an arrangement of heterovalent Mn should provide a similar degree of undersaturation for layer O atoms. As can be seen in Figure 16, O atoms coordinated by two Mn^{3+} and one Mn^{4+} will form two short Mn^{3+}-O bonds and one long Mn^{4+}-O bond. Oxygen atoms coordinated

by two Mn^{4+} and one Mn^{3+} will form two short Mn^{4+}-O bonds and one very long Mn^{3+}-O bond. The different dimensions of Mn^{3+} and Mn^{4+} rows along the A axis are the main reason for the deviation of NaBi and SrBi layers from the hexagonal symmetry. Figure 16 shows that Mn^{3+} and Mn^{4+} octahedral rows alternate regularly along the A axis in the sequence $Mn^{3+}Mn^{4+}Mn^{4+}Mn^{3+}$ leading, together with the ordered distribution of interlayer Na and H_2O, to a supercell with $A = 3a$ and $B = 3b$. The maximum proportion of Mn^{3+} is then 0.33. Additional support for this model comes from the Na:Mn ratio for NaBi equal to 0.33, which is consistent with a 1:1 Na:Mn^{3+} ratio. This structural model allows us to explain the main experimental diffraction features. First, the origin of the supercell parameter $A = 3a$ for NaBi and SrBi is evident. Second, without the assumption of Mn^{3+} ordering it is difficult to explain why Na and Sr cations, which differ in valence, size, and hydrolysis properties, occupy the same crystallographic positions within the unit cell with $A = 3a$ and $B = b$ or $B = 3b$. In the absence of Mn^{3+} rows the distribution of interlayer cations described previously for these microcrystal types would probably not be the lowest energy configuration. The high concentration of Na and Sr cations along Mn^{3+} rows can be justified only if they are forced in this arrangement to provide a local charge compensation (e.g., Fig. 10). Finally, if the formation of layer vacancies during the NaBi to HBi transformation results from the migration of Mn^{3+} from layer to interlayer sites thus forming layer vacancies ($Mn^{3+}_{layer} \rightarrow \square_{layer} + Mn^{3+}_{interlayer}$), then the distribution of layer vacancies should reflect the former distribution of Mn^{3+}. As a consequence, layer vacancies should also be ordered according to the supercell with $A = 3a$ and $B = b$. As mentioned previously, the superposition along c of interlayer Mn and vacant layer sites strongly weakens the intensity of $hk0$ superreflections. However, interlayer H_2O molecules coordinated to interlayer Mn are distributed in the same way as vacant sites and enhance this intensity slightly. This regular distribution of interlayer species according to the predicted unit cell (Fig. 2c) confirms that layer vacancy distribution reflects the distribution of Mn^{3+} in the original NaBi structure.

Structure of the Na-rich birnessite interlayer

In both types of NaBi superstructures, adjacent layers are shifted by $-0.327a$ and the super-cells have a common periodicity of $A = 3a$. However, they differ by their B periodicity. In this section the interlayer structure of both types of NaBi is described in detail. The total layer charge and the mutual arrangement of Mn^{4+}/Mn^{3+} cations can then be derived.

NaBi type II: Supercell with $A = 3a$, $B = 3b$, and $\gamma = 90°$. The cell shown in Figure 17 contains six Na atoms each of which surrounded by six H_2O molecules. The cation content is $Na_{0.33}Mn^{4+}_{0.67}Mn^{3+}_{0.33}$. Due to the ordered distribution of Mn^{4+} and Mn^{3+}, successive rows of O atoms are coordinated to two Mn^{3+} and one Mn^{4+}, to two Mn^{4+} and one Mn^{3+}, and to three Mn^{4+}. These different
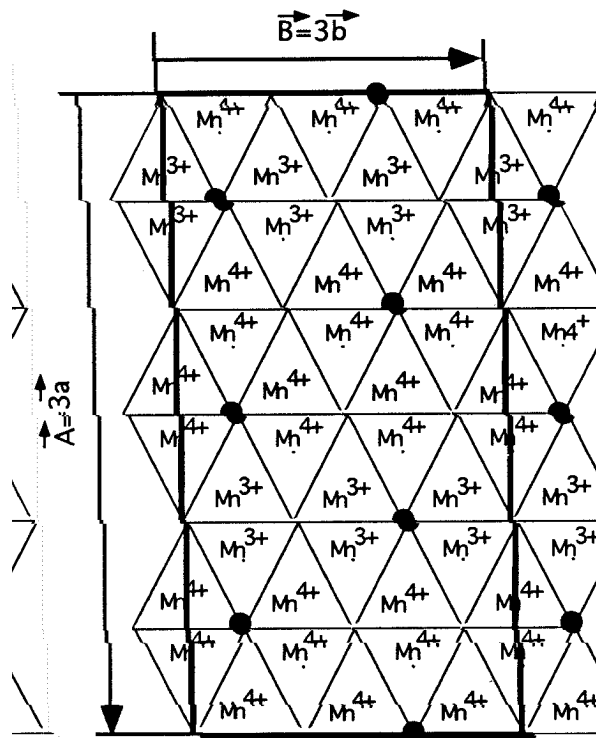
FIGURE 17. Mutual arrangement of Mn^{3+} and Mn^{4+} in two adjacent layers within the supercell with $A = 3a$ and $B = 3b$ in the idealized case where $c \cos\beta / a = -0.333$ instead of the observed value of -0.327. Large solid circles represent Na sites. The corner of the triangles correspond to overlapping O atoms of the adjacent layers. Na and H_2O are distributed along b according to the sequence Na-H_2O-H_2O-Na. . . .

O atoms differ by their degree of undersaturation of positive charge. Accordingly, Na cations will possess different bonding strength with nearest O atoms. Figure 17 shows that two-thirds of Na cations are located between two saturated O atoms of adjacent layers whereas the other third of Na cations are associated with undersaturated O atoms.

NaBi type I: Supercell with $A = 3a$, $B = b$, and $\gamma = 90°$. Let us assume (1) that all Na atoms associated with Mn^{3+} are placed only in rows separated from each other by distances of $A/2$ along the A axis and are distributed according to the sequence Na-H_2O-Na-H_2O. . . and (2) that the rows are shifted at random relative to each other by $\pm^b/_2$ (Fig. 18). Such an arrangement of interlayer species leads to $B = b$ as observed experimentally. The maximum amount of Na and Mn^{3+} per cell is then equal to one atom and the cationic composition corresponds to $Na_{0.167}Mn^{4+}_{0.833}Mn^{3+}_{0.167}$. In this structural model, Mn^{3+}-rich rows now contain only 50% of Mn^{3+}. As can be seen in Figure 18, any additional Na in rows adjacent to Mn^{3+}-rich rows results in the formation of Na-Na pairs at distances of 2.85 Å. To increase the amount of Na and Mn^{3+} within the same supercell from 0.167 up to 0.20–0.25 atoms per octahedron, Na and H_2O would have to
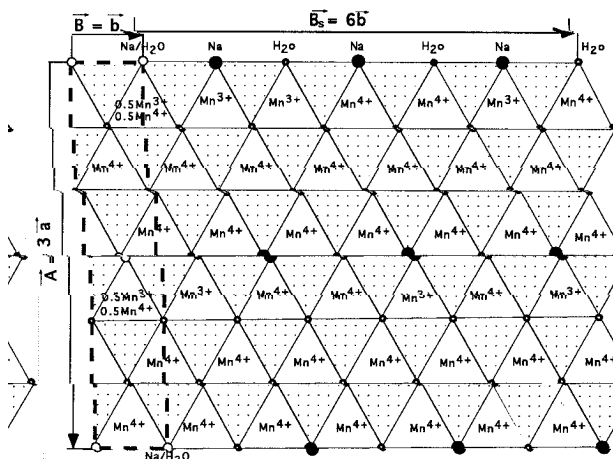
FIGURE 18. Model for the ordered distribution of Na and H_2O along b axis, with the sequence Na-H_2O-Na-H_2O-Na. . . The rows containing Na and H_2O are separated from each other by $A/2$ along the A axis and are displaced at random by $\pm\frac{b}{2}$. Na: Mn^{3+} ratio is 1:6.

FIGURE 19. Periodic distribution of Mn^{4+} and Mn^{2+} along Mn^{3+}-rich rows in the supercell with $A = 3a$ and $B = \lambda = 6b$. The periodic distribution of Na (solid circles) and H_2O (open circles) with $A = 3a$ and $B = 3b$ supercell parameters is also shown.

alternate along the rows in a disordered way (e.g., Na-H_2O-Na-H_2O-H_2O-Na-H_2O. . .). In layer domains with a negative charge greater than 0.167 v.u. per octahedron, Na associated with Mn^{3+}-rich rows should exhibit Na-H_2O-H_2O-Na subsequences. In this case additional Na may be placed between Mn^{3+}-rich rows to provide the layer charge compensation and to avoid Na-Na pairs at distances of 2.85 Å.

S cell. In spite of the different superstructures, both NaBi types have a common periodicity along b for the structural modulations leading to the appearance of satellites. Several models may be proposed to explain this structural feature of NaBi. For instance, one may assume that within the Mn^{3+} rows there is a regular substitution of Mn^{4+} for Mn^{3+} according to the sequence Mn^{4+}-$5Mn^{3+}$-Mn^{4+}-$5Mn^{3+}$. Such an ordered distribution of Mn^{3+} and Mn^{4+} results in an S cell with $A_s = 3a$ and $B_s = 6$. This ordered sequence of heterovalent Mn cations should lead to a periodic distribution of interlayer cations along the b axis and therefore to a modulation of d. It is easy to calculate that the S cell contains 26 Mn^{4+} and 10 Mn^{3+}, which corresponds to an Mn^{4+} content of 0.723 per octahedral site. This value is close to the experimental value of 0.734 (Silvester et al. 1997). Another way to create a periodic charge distribution along Mn^{3+} rows results from Mn^{3+} disproportionation. Let us assume that with the periodicity $\lambda = 6b$ two Mn^{3+} cations transformed in one Mn^{4+} and one Mn^{2+} (Fig. 19). Within the supercell there would be 26 Mn^{4+}, 8 Mn^{3+}, and 2 Mn^{2+} within the layer. According to this extreme case the cationic composition of NaBi calculated per octahedron can be written $Na_{0.333}(Mn^{4+}_{0.722}Mn^{3+}_{0.223}Mn^{2+}_{0.055})$. Again, different values of negative charge distributed periodically in Mn^{3+}-rich rows should lead to a periodic variation of interlayer cation contents and of d values. The same effect should be
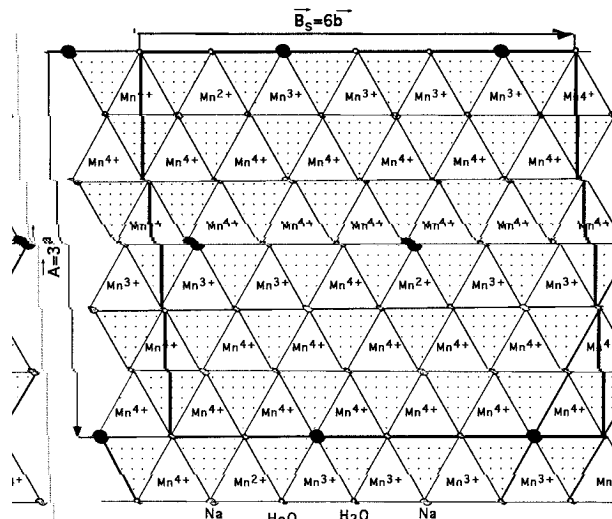
observed if Mn^{2+} migrates in the interlayer with simultaneous formation of vacant layer sites. This structural formula obtained for NaBi is very close to that derived independently from solution chemistry (Silvester et al. 1997).

The present structural model for monoclinic birnessite presents some similarities with that of Kuma et al. (1994). Both are based on a linear distribution of negative charges. However, Kuma et al. (1994) assumed that the negative layer charge results only from layer vacancies, and they did not consider the possibility of heterovalent Mn cations in layers. In contrast, the present model assumes that the source of negative charge is due mostly to layer Mn^{3+}, the density of layer vacancies being low, if any. Furthermore, it offers the advantage of accounting for the large value of the a parameter and its decrease upon the formation of layer vacancies through either cation exchange, direct oxidation of Mn^{3+} and Mn^{2+}, or NaBu to NaBi transformation by means of the Mn^{3+} disproportionation. In addition, this model allows the derivation of all experimental electron diffraction patterns (Figs. 2 and 5) by introducing only slight displacements of interlayer cations from their ideal positions described by the supercell with $A = 3a$ and $B = b$.

Structural heterogeneity of birnessite

Whatever the interlayer cation, synthetic birnessite samples usually exhibit two or three different types of SAED patterns. Several reasons can be suggested for this diversity of diffraction patterns, including the density of the layer charge, the nature and distribution of heterovalent cations in layers, and the nature of interlayer cations.

NaBi. We assumed that microcrystals having the unit

cell $A = 3a$ and $B = 3b$ have a higher layer charge than microcrystals with $A = 3a$ and $B = b$. Two opposing forces control the distribution of interlayer cations: (1) their tendency to distribute homogeneously to minimize their electrostatic repulsion and (2) the requirement of providing local charge compensation. For microcrystals with a relatively low charge, the latter situation seems to dominate (NaBi type I), whereas at high layer charge interlayer cations tend to distribute homogeneously (NaBi type II). However, it is noticeable that in both NaBi varieties the origin of satellites is the same: They appear as the result of the periodic variation of interplanar spacing along [01] with the same wavelength of $\lambda = 6b$. This result supports the idea that the Mn^{3+}-Mn^{4+} distribution along Mn^{3+}-rich rows is independent of the layer charge.

SrBi. The diversity of SAED patterns is greater with SrBi than with NaBi. This observation indicates that structural heterogeneities of layers caused by lateral variations of charge (i.e., distribution of heterovalent cations) are more easily achieved with Sr because of its large ionic radius, smaller content, and divalent character. In contrast to Na, Sr cations are shifted along the normal to $(\overline{3}10)$ planes (Figs. 13 and 14). The displacement in this direction most likely reduces the electrostatic repulsion between divalent cations. The varying periodicity of $d_{\overline{3}10}$ possibly reflects variations in the layer charge as well as some variation in Mn^{3+} and Mn^{4+} ordering. In contrast to NaBi, the regular structural fluctuation along the normal to $(\overline{3}10)$ does not lead to a fluctuation of d_{010} despite the fact that Sr cations are placed on the planes parallel to (010). This effect comes from the fact that the projection on the b axis of all individual displacements of Sr atoms, from their ideal position with a given y coordinate, is equal to zero when averaged over a $4A$ period.

It is worth mentioning that twins of SrBi microcrystals exhibit a strict periodicity. It is likely that the most stable structure, with a complete local compensation of layer charge, occurs when the position of Sr cations in two nearest interlayers are connected by a glide plane (Fig. 15). The last variety of SrBi is characterized by a primitive unit cell with $A = 3a$ and $B = 4b$. As can be seen in Figure 10, Sr cations are localized in the same level along the A axis as in all other structural varieties. The peculiar distribution of Sr most probably reflects a specific ratio and periodicity of Mn^{3+} and Mn^{4+} along Mn^{3+}-rich rows.

REFERENCES CITED

Balistrieri, L.S. and Murray, J.W. (1982) The surface chemistry of δMnO₂. Geochimica et Cosmochimica Acta, 46, 1041–1052.
Bidoglio, G., Gibson, P.N., O'Gorman, M., and Roberts, K.J. (1993) X-ray absorption spectroscopy investigation of surface redox transformations of thallium and chromium on colloidal mineral oxides. Geochimica et Cosmochimica Acta, 57, 2389–2394.
Bricker, O. (1965) Some stability relations in system Mn-O₂-H₂O at 25 °C and one atmosphere total pressure. American Mineralogist, 50, 1296–1354.
Burns, R.G. and Burns, V.M. (1976) Mineralogy of ferromanganese nodules. In G.P. Glasby, Ed., Marine manganese deposits, p. 185–248. Elsevier, Amsterdam.
——— (1977) The mineralogy and crystal chemistry of deep-sea manganese nodules, a polymetallic resource of the twenty-first century. Philosophical Transactions of the Royal Society of London (A), 286, 283–301.
Chukhrov, F.V. and Gorshkov, A.I. (1981) Iron and manganese oxide minerals in soils. Transactions of the Royal Society of Edinburgh, 72, 195–200.
Chukhrov, F.V., Gorschkov, A.I., Rudnitskaya, E.S., and Sivtsov, A.V. (1978) Birnessite characterization. Investiya Akademie Nauk, SSSR, Seriya Geologicheskaya, 9, 67–76.
Chukhrov, F.V., Sakharov, B.A., Gorshkov, A.I., Drits, V.A., and Dikov, Y.P. (1985) Crystal structure of birnessite from the Pacific Ocean. International Geology Review, 27, 1082–1088 (translated from Investiya Akademie Nauk, SSSR, Seriya Geologicheskaya, 8, 66–73).
Chukhrov, F.V., Gorshkov, A.I., Berezovskaya, V.V., and Sivtsov, A.V. (1987) New data about mineralogy of Kertch ore deposits. Investiya Akademie Nauk, SSSR, Seriya Geologicheskaya, 4, 60–77.
Chukhrov, F.V., Gorshkov, A.I., and Drits, V.A. (1989) Supergenic manganese hydrous oxides, 208 p. Nauka, Moscow.
Cornell, R.M. and Giovanoli, R. (1988) Transformation of hausmannite into birnessite in alkaline media. Clays and Clay Minerals, 36, 249–257.
Drits, V.A. (1987) Electron diffraction and high resolution electron microscopy of mineral structures, 304 p. Springer-Verlag, Berlin.
Drits, V.A., Petrova, V.V., and Gorshkov, A.I. (1985) Manganese minerals of Fe-Mn nodules from the sediments of the central part of Pacific Ocean and their post-sedimentation transformation. Lithology and Raw Materials, 3, 17–39.
Giovanoli, R. and Arrhenius, G. (1988) Structural chemistry of marine manganese and iron minerals and synthetic model compounds. In P. Halbach, G. Friedrich, and U. von Stackelberg, Eds., The manganese nodule belt of the Pacific Ocean: Geological environmental, nodule formation, and mining aspects, p. 20–37. Verlag, Stuttgart.
Giovanoli, R., Stähli, E., and Feitknecht, W. (1970a) Über Oxidhydroxide des vierwertigen Mangans mit Schichtengitter. 1. Mitteilung: Natriummangan(II,III)manganat(IV). Helvetica Chimica Acta, 53, 454–464.
——— (1970b) Über Oxidhydroxide des vierwertigen Mangans mit Schichtengitter. 2. Mitteilung: Mangan(III)-manganat(IV). Helvetica Chimica Acta, 53, 454–464.
Giovanoli, R., Feitknecht, W., Maurer, R., and Hani, H. (1976) Homogene Keimbildung und Keimwachstum von γMnO₂. Chimia, 30, 268–269.
Glover, E.D. (1977) Characterization of a marine birnessite. American Mineralogist, 62, 278–285.
Gorshkov, A.I., Drits, V.A., Putilita, V.S., Pokrovskaya, E.V., and Sivtsov, A.V. (1992) Natural and synthetic birnessites. Lithology and Raw Materials, 6, 67–81.
Healy, T.W., Herring, A.P., and Fuerstenau, D.W. (1966) The effect of crystal structure on the surface properties of a series of manganese dioxides. Journal of Colloid and Interface Science, 21, 435–444.
Jones, L.H.P. and Milne, A.A. (1956) Birnessite, a new manganese oxide mineral from Aberdeenshire, Scotland. Mineralogical Magazine, 31, 283–288.
Kuma, K., Usui, A., Paplawsky, W., Gedulin, B., and Arrhenius, G. (1994) Crystal structures of synthetic 7 Å and 10 Å manganates substituted by mono- and divalent cations. Mineralogical Magazine, 58, 425–447.
Le Goff, P., Baffier, N., Bach, S., and Pereira-Ramos, J.P. (1996) Synthesis, ion exchange and electrochemical properties of lamellar phyllomanganates of the birnessite group. Material Research Bulletin, 31, 63–75.
Manceau, A. and Charlet, L. (1992) X-ray absorption spectroscopic study of the sorption of Cr(III) at the oxide-water interface. Journal of Colloid and Interface Science, 148, 425–442.

Manceau, A., Gorshov, A.I., and Drits, V.A. (1992) Structural chemistry of Mn, Fe, Co and Ni in manganese hydrous oxides: Part II. Information from EXAFS spectroscopy and electron and X-ray diffraction. American Mineralogist, 77, 1144–1157.

Murray, J.W. (1974) The surface chemistry of hydrous manganese dioxide. Journal of Colloid and Interface Science, 46, 357–371.

Paterson, E., Swaffield, R., and Clark, L. (1994) The influence of structure on Ba and K uptake by a synthetic phyllomanganate. Clay Minerals, 24, 215–222.

Post, J.E. and Appleman, D.E. (1988) Chalcophanite, $ZnMn_3O_7.3H_2O$: New crystal structure determinations. American Mineralogist, 73, 1401–1404.

Post, J.E. and Veblen, D.R. (1990) Crystal structure determinations of synthetic sodium, magnesium, and potassium birnessite using TEM and the Rietveld method. American Mineralogist, 75, 477–489.

Silvester, E., Manceau, A., and Drits, V.A. (1997) The structure of monoclinic Na-rich birnessite and hexagonal birnessite: II. Results from Chemical Studies and EXAFS Spectroscopy. American Mineralogist, 82, 962–978.

Stone, A.T. (1987) Reductive dissolution of manganese (III,IV) oxides by substituted phenols. Environmental Science and Technology, 21, 979–988.

Stone, A.T. and Morgan, J.J. (1984) Reductive dissolution of manganese (III) and manganese (IV) oxides by organics. Environmental Science and Technology, 18, 617–624.

Stone, A.T., Godtfredsen, K.L., and Deng, B. (1994) Sources and reactivity of reductant encountered in aquatic environments. In G. Bidoglio and W. Stumm, Eds., Chemistry of aquatic systems: Local and global perspectives, p. 337–374. EURO courses series.

Strobel, P., Charenton, J.C., and Lenglet, M. (1987) Stuctural chemistry of phyllomanganates: Experimental evidence and structural models. Revue de Chimie Minérale, 24, 199–220.

Taylor, R.M., McKenzie, R.M., and Norrish, K. (1964) The mineralogy and chemistry of manganese in some Australian soils. Australian Journal of Soil Research, 2, 235–248.

Töpfer, J., Trari, M., Gravereau, P., Chaminade, J.P., and Donmerc, J.P. (1995) Crystal growth and re-investigation of the crystal structure of crednerite, $CuMnO_2$. Zeitschrift für Kristallographie, 210, 184–187.

Tu, S., Racz, G.J., and Goh, T.B. (1994) Transformation of synthetic birnessite as affected by pH and manganese concentration. Clays and Clay Minerals, 42, 321–330.

Usui, A. and Mita, N. (1995) Geochemistry and mineralogy of a modern buserite deposit from a hot spring in Hokkaido, Japan. Clays and Clay Minerals, 43, 116–127.

Wadsley, A.D. (1955) The crystal structure of chalcophanite, $ZnMn_3O_7.3H_2O$. Acta Crystallographica, 8, 165–172.

Wilson, A.J.C. (1964) X-ray optics: The diffraction of X-rays by finite and imperfect crystals, 147 p. Wiley, New York.

Xyla, A.G., Sulzberger, B., Luther, G.W., Hering, J.G., Van Capellen, P., and Stumm, W. (1992) Reductive dissolution of manganese(III,IV) (hydr)oxides by oxalate: The effect of pH and light. Langmuir, 8, 95–103.